RSC Advances

ROYAL SOCIETY OF CHEMISTRY

PAPER

View Article Online
View Journal | View Issue

Check for updates

Cite this: *RSC Adv.*, 2024, **14**, 12454

Fluorinated carbon as high-performance cathode for aqueous zinc primary batteries†

Congping Xu, [abc] Liang Zhang,[d] Fupeng Liu,*[a] Ruding Zhang *[bc]
and Hongjun Yue*[bc]

Received 1st February 2024
Accepted 7th April 2024

DOI: 10.1039/d4ra00835a

rsc.li/rsc-advances

Fluorinated carbon (CF_x) has been extensively served as promising positive electrode material for lithium primary batteries due to its high energy density. However, there are comparatively far less reports about the use of CF_x on other battery systems, let alone on the research of aqueous batteries. Herein in this study, we employed CF_x as the cathode active for aqueous zinc batteries for the first time and systematically investigated its electrochemical behavior under a series of aqueous zinc-ion electrolytes. As is discovered that the F/C ratio (the x value in CF_x) of CF_x have significant effects on the electrochemical performance of aqueous Zn/CF_x batteries. Specifically, $CF_{0.85}$ exhibits excellent electrochemical property with delivering a remarkable discharge capacity of 503 mA h g^{-1} and energy density of 388 W h kg^{-1} (at a current rate of 30 mA g^{-1} under temperature of 25 °C), much better than several other CF_x electrode with F/C ratio of 0.70, 0.95, and 1.10, respectively. Besides, it also exhibits decent temperature performance with discharge capacities of 550 mA h g^{-1} at 50 °C and 460 mA h g^{-1} at 0 °C under current density of 30 mA g^{-1}. Furthermore, the electrochemical discharge mechanism based on conversion reaction was further uncovered by applying XPS, XRD, SEM and EDS elemental analysis characterization techniques. In conclusion, these results demonstrate the potential application value of CF_x in aqueous zinc primary batteries.

1. Introduction

As is well known, secondary lithium-ion batteries occupy a dominant position in the entire battery industry due to the advantages of their rechargeability, high energy density, and good cycling performance during recent years. On the contrary, much less research attention has been paid to primary battery systems. However, given their unique historical status, the application potential of primary batteries should not be disregarded in certain special fields and extreme scenarios.[1,2] Among all primary battery systems, Li/CF_x primary batteries hold a place of great importance owing to their remarkable discharge voltage platform, impressive energy density and wide operating temperature range. They have been extensively utilized in cutting-edge fields including medical devices, military weapons, and aerospace areas.[1,3–5] However, with the continuous expansion of the application field of lithium batteries, the fact of the scarcity and uneven distribution of lithium resources has caused a constant increase in its price.[6] Thus, it is imperative to develop other low-cost electrochemical energy storage systems with considerable performance and without using lithium. On the basis of above analysis and consideration, non-lithium primary batteries based CF_x cathode such as Na/CF_x, K/CF_x, Mg/CF_x and Al/CF_x batteries have been favored by researchers. For example, Fu *et al.*[7] demonstrated the feasibility of CF_x cathode in sodium-ion batteries. Similarly, Yue *et al.*[8] reported on the usage of CF_x as a high capacity conversion-type cathode for potassium batteries, and further investigated the mechanism of this highly reversible conversion reaction through nuclear magnetic resonance spectroscopy, X-ray diffraction, and transmission electron microscopy. In addition, researchers have also reported on Mg/CF_x and Al/CF_x systems. For instance, Vatsala Rani J. *et al.*[9] successfully electrochemically fluoridated natural graphite with triethylamine tri(hydro fluoride) $(C_2H_5)_3N.3HF$ adduct, and then used it in magnesium batteries. The resulting CF_x cathode, when combined with a magnesium anode, exhibited rechargeability. However, specific details regarding the reaction mechanism, particularly the formation and destruction of Mg–F bonds, remain unclear. Although the above battery systems

---

[a] Faculty of Materials Metallurgy and Chemistry, Jiangxi University of Science and Technology, Ganzhou 341000, Jiangxi, China. E-mail: fupengliu@126.com

[b] CAS Key Laboratory of Design and Assembly of Functional Nanostructures, Fujian Provincial Key Laboratory of Nanomaterials, Fujian Institute of Research on the Structure of Matter, Chinese Academy of Sciences, Fuzhou 350002, China. E-mail: rdzhang@fjirsm.ac.cn; hjyue@fjirsm.ac.cn

[c] Xiamen Institute of Rare-earth Materials, Haixi Institutes, Chinese Academy of Sciences, Xiamen 361021, China

[d] State Key Laboratory of Advanced Chemical Power Sources, Guizhou Meiling Power Sources Co.Ltd, Zunyi 563003, China

† Electronic supplementary information (ESI) available. See DOI: https://doi.org/10.1039/d4ra00835a

have a relatively high discharge voltage and specific capacity, but they must use high-toxic organic electrolyte with low safety factor, and assembly environment requirements is also demanding. Additionally, the fact that high active metals such as lithium, sodium, potassium, and magnesium are directly used as the negative electrode not only makes the operation complicated but also exists considerable safety risks. It is universally acknowledged that aqueous zinc-based batteries possess outstanding advantages such as intrinsic safety, high ionic conductivity of aqueous electrolyte and can be directly assembled in the surrounding air environment, showing a vast application prospect in the field of electrochemical energy storage.[10–14] Meanwhile, extensive literature research indicates no current reports on the utilization of CF_x electrode materials in aqueous zinc-based battery systems. Considering the high electrochemical performance of Li/CF_x batteries, it is reasonable to expect CF_x active materials to demonstrate comparable electrochemical reactivity in aqueous zinc-based batteries.

In this work, CF_x materials were used for the first time as cathode electrode active materials in aqueous zinc primary batteries, and their electrochemical behaviors were systematically investigated in a range of aqueous zinc-ion electrolytes. The result shows that the F/C ratio of CF_x significantly influenced the electrochemical performance of aqueous Zn/CF_x batteries. Among them, $CF_{0.85}$ exhibited the best electrochemical performance, with a discharge capacity of 503 mA h g^{-1} and an energy density of 388 W h kg^{-1}. The electrochemical performance of $CF_{0.85}$ was also tested at 0 °C and 50 °C with discharge capacities of 460 mA h g^{-1} and 550 mA h g^{-1}, respectively. This indicates its ability to function properly in common harsh environments. Furthermore, XRD, SEM, and EDS elemental analysis characterization techniques were employed to further reveal the electrochemical discharge mechanism based on conversion reactions.

2. Experimental section

2.1 Materials

Commercially available CF_{070}, $CF_{0.85}$, $CF_{0.95}$ and $CF_{1.10}$ were provided by Xiamen Zhong Ke Ceffone Technology Co., Ltd without further treatment.

2.2 Electrochemical test

The working electrodes were fabricated by spreading the slurry of the active materials (80 wt%), conductive carbon black (10 wt%), and polyvinylidene fluoride (PVDF, 10 wt%) dispersion in *N*-methyl-pyrrolidinone (NMP) onto stainless steel-304 net, and then dried in a vacuum oven at 80 °C overnight to remove the solvent. Typical mass loading was 2–3 mg cm^{-2}, high mass loading was 6–7 mg cm^{-2}. All the electrochemical tests were conducted in coin cells (CR2025). The coin cells were assembled with zinc metal as a counter electrode, 4 M $Zn(CF_3SO_3)_2$/3 M $ZnSO_4$/2 M $Zn(CH_3COO)_2$ aqueous solution as electrolytes, and glass fiber as a separator in the air. Coin cells were discharged on a Neware battery test system (MIHW-200-160CH) at a temperature of 25 °C, low temperature and high temperature performance tests were conducted in a high and low temperature test chamber (HDGDW-50; Shanghai Hengding Instrument & Equipment Factory). The cut-off potential was set at 0.3 V (*vs.* Zn/Zn^{2+}). Cyclic voltammetry (CV), galvanostatic intermittent titration technique (GITT), and electrochemical impedance spectroscopy (EIS) were performed by an electrochemical workstation (Shanghai Chenhua CHI 760e, China). EIS test was performed at an open-circuit voltage (OCV) with an AC amplitude of 5 mV and a frequency range of 100 kHz–10 mHz. For galvanostatic intermittent titration technique (GITT) analyses, the cells discharged at a current density of 30 mA g^{-1}. The duration times of 5 and 50 min were applied for each applied galvanostatic current and rest, respectively.

2.3 Material characterizations

Powder and electrode X-ray diffraction (XRD) patterns were collected by Miniflex 600 from 5 to 80°(2θ) at a scan speed of 5° min^{-1}, using Cu Kα radiation ($\lambda = 1.5406$ Å) operated at 40 kV and 15 mA. Morphological features were obtained by an Apreo S LoVac scanning electron microscope (SEM), operating at 200 kV. Raman spectrometry (Horiba Jobin Yvon S.A.S., LabRAM Aramis) using a laser with a wavelength of 532 nm. The FTIR spectra were obtained with a Fourier transform infrared spectrometer (Thermo Fisher, Nicolet iS 50). The UV-vis measurement was performed by the Agilent Cary 500 with a wavelength range of 200 nm to 800 nm. The X-ray photoelectron spectroscopy (XPS) analysis was performed by Thermo fisher Scientific K-Alpha with monochromatic Al Kα source. To acquire the specific surface areas and pore volume of samples, the N_2 adsorption/desorption characteristics were measured by Autosorb-iQ at 77 K.

3. Results and discussion

The optical images of $CF_{0.70}$, $CF_{0.85}$, $CF_{0.95,}$ and $CF_{1.10}$ samples are shown in Fig. 1a. As the F/C ratio increased, the color of the four samples gradually changed from black to white. As shown by the UV-vis spectra (Fig. S1†), with the increase of the F/C ratio, the intensity of the absorption peak at 280 nm gradually decreases and red shifted. This is due to the highly covalent nature of C–F bonds formed during fluorination at high temperatures, which causes a reduction in the aromaticity of CF_x and results in a white product.[15,16] On the other hand, as the fluorination temperature decreases, the color of CF_x gradually changes from gray to black.[17,18] Fig. 1b dispiays the XRD patterns of four CF_x materials, exhibiting two characteristic broad peaks that corresponding to the fluorinated phases (2$\theta \approx$ 13° and 41°).[19,20] The diffraction peaks located around 13° and 41° belong to the characteristic diffraction peaks of CF_x materials, and the former characteristic diffraction peaks could be indexed in a hexagonal system as the (001) reflection. The peak around 41° corresponds to the (100) lattice plane and is attributed to the C–C in-plane length in the reticular system. The sharper the XRD diffraction peak, the higher the crystallinity of the material, the order of the crystallinity of the four CF_x from high to low is $CF_{1.10}$, $CF_{0.95}$, $CF_{0.85}$ and $CF_{0.70}$. As the

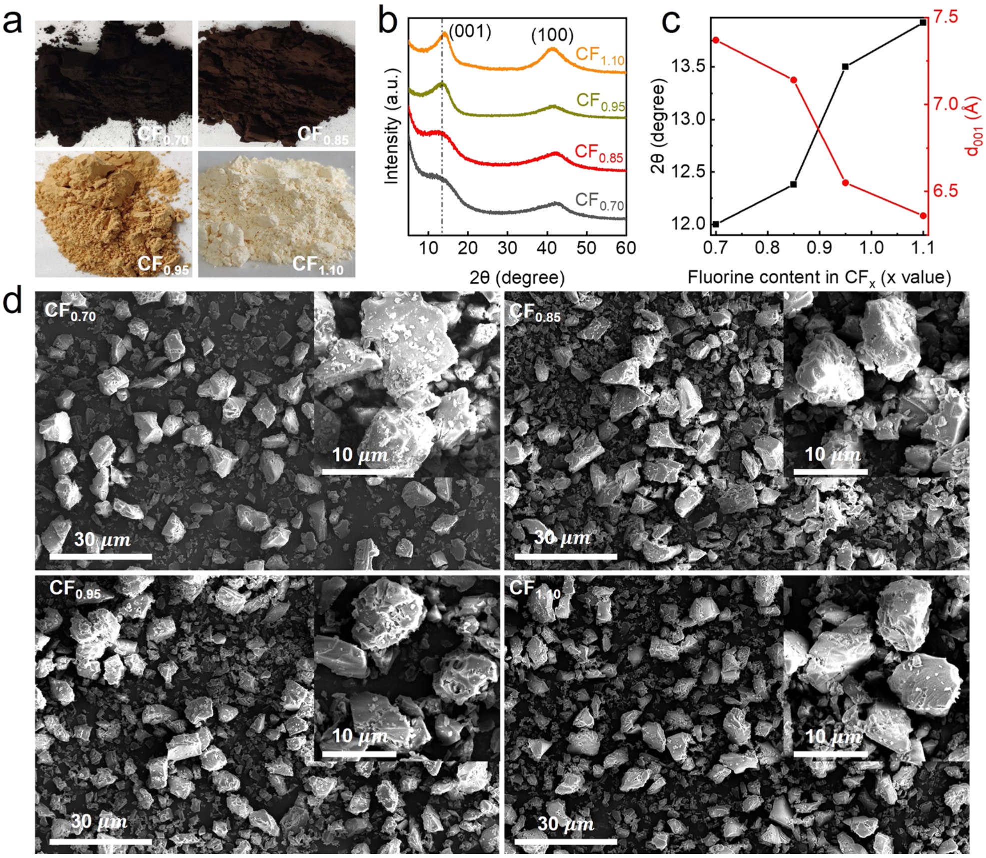

Fig. 1 (a) Images of the CF_x. (b) XRD patterns of the CF_x, (c) the degree and interlayer distance of the (001) diffraction peak. (d) SEM images of the samples.

temperature of fluorination increases, the (100) reflection shifts to the lower angle, indicating an increase in the length within the C–C plane, which means more and more C and F atoms combine to form CF_x compounds and is consistent with the trend of fluorinated graphite. In addition, the (001) reflection peak corresponds to the hexagonal system compound with high fluorine content becoming more pronounced at higher temperatures, indicating that more carbon layers are fluorinated.[21] Fig. 1c shows the plots of degree and interlayer distance (d_{001}) for the samples from the (001) diffraction peak in their XRD patterns. The 2θ value for (001) peaks is 12.00, 12.38, 13.50, and 13.92 for $CF_{0.70}$, $CF_{0.85}$, $CF_{0.95}$ and $CF_{1.10}$. When the F/C ratio increased from 0.70 to 1.10, the diffraction peaks gradually shift to a high degree, and the d_{001} has the opposite trend. Fig. 1d displays the scanning electron microscopy (SEM) images of CF_x powders. The images present an irregular block morphology, and fine flake substances are attached to the surface of the block, which may be due to the destruction of the original structure of the carbon source by fluorine gas during the fluorination process, resulting in the production of these fine flake substances. The particle size of CF_x is between 1–10 μm. The FT-IR is used to investigate the chemical structure of the four CF_x samples, and the result is shown in Fig. S2.† The intense absorption peak observed at around 1210 cm^{-1} is assigned to the covalent C–F bond. It can be found that with the increase of fluorination temperature, there is a blue shift of C–F bonds in the FT-IR spectrum of CF_x, and the full width at the half peak narrows and the peak intensity becomes stronger, indicating that the bonding strength between C and F atoms has increased.[22–24] The absorption peaks located near 1328 cm^{-1} and 660 cm^{-1} are characteristic of the CF_2 group and CF_3 group, respectively, and their intensity increases with increasing fluorination temperature. In addition, the peak at 1100 cm^{-1} indicates the semi-covalent C–F bond and weakens as the fluorination temperature rises.[25] Fig. S3† shows the Raman spectrum of CF_x. In the case of $CF_{0.70}$ and $CF_{0.85}$, two distinct Raman resonance peaks are observed. The former peak corresponds to the D band, which is generated by disordered sp^3 carbon bonding, while the latter is the G band, which occurs due to the in-plane bond stretching of sp^2 carbons in carbon materials.[26,27] The presence of the G band in $CF_{0.70}$ and $CF_{0.85}$ suggest the existence of some sp^2-hybridized carbon domains in the material due to a relatively low degree of fluorination. However, $CF_{0.95}$ and $CF_{1.10}$ with high fluorine content do not exhibit any clear Raman band due to strong fluorescence.[8,28]

The surface characterizations of materials were determined by N_2 adsorption–desorption isotherm measurements. As shown in Fig. S4a,† it can be found that all the isotherms present similar type IV shape, and exhibit a hysteresis loop typical of a mesoporous, which demonstrated that large amounts of micropores and mesopores existed in samples.[29] According to the isotherm, the specific surface areas of $CF_{0.70}$,

$CF_{0.85}$, $CF_{0.95}$ and $CF_{1.10}$ are 592.3 $m^2\ g^{-1}$, 564.8 $m^2\ g^{-1}$, 370.4 $m^2\ g^{-1}$ and 291.5 $m^2\ g^{-1}$, respectively. The electrochemical performance of the two samples with high fluoridation is also poor due to the sharp decrease in specific surface area. As shown in Fig. S4b,† CF_x are mainly microporous and mesoporous structures, which proves the etching effect of fluorine. Samples with large specific surface area and abundant pores can supply more active sites and guarantee the rapid diffusion for Zn^{2+} in the discharge reaction.

The composition and functional species of CF_x were further measured by XPS. As shown in Fig. S5a–d,† the peaks at about 284.8 and 688.08 eV demonstrate the existence of C and F elements. To get the further insights of the types of C–F bonds, high resolution XPS of C 1s and F 1s surveys were conducted, respectively. In C 1s spectra (Fig. S5e–h†), the peaks of C–F bonds increase with the F/C ratio, while the peaks of C=C bonds gradually reduce. The sp^2 C–C is still maintained in all CF_x, which is helpful to reduce charge transfer resistance. With the increase of F/C ratio, the intensity of per-fluorinated groups like $-CF_2$ increase, these non-electrochemically active and electrical insulation groups will significantly decrease the specific capacity and discharge potential of materials with high F/C ratio.[30] In the F 1s spectra (Fig. S5i–l†), the deconvoluted peaks with binding energy ranked from high to low were attributed to the fluorinated species of per-fluorinated $-CF_2$, covalent F–C, and semi-ionic F–C configurations.[28]

To investigate the electrochemical performances of prepared CF_x as the cathodes of Zn/CF_x batteries, galvanostatic discharge tests were conducted at various discharge rates. The performance of $CF_{0.85}$ and $CF_{0.95}$ with $ZnSO_4$ and $Zn(CH_3COO)_2$ conventional electrolytes, as illustrated in Fig. S6,† were poor and are not enough to give full play to the electrochemical performance of CF_x materials, so we chose saturated $Zn(CF_3SO_3)_2$ aqueous solution as electrolytes often used in zinc ion batteries to evaluate its performance.[31] Fig. S7† shows the cyclic voltammetry (CV) curves recorded for the Zn/CF_x in $Zn(CF_3SO_3)_2$ aqueous electrolytes. The curves present widened reduction peaks when scanned negatively and no any oxidation peak when scanned positively, indicating an irreversible electrochemical reaction between zinc ion and CF_x. Relatively, the $CF_{0.85}$ cathode exhibits larger peak currents in $Zn(CF_3SO_3)_2$ electrolyte than other CF_x, which suggests stronger redox reactions occurred in $Zn/CF_{0.85}$ cells. This is supported by galvanostatic discharge measurements. Due to the extremely poor performance of $CF_{1.10}$, it leads to rapid diffusion on a time scale, so that the electrolyte solution and the electrode surface can quickly reach an equilibrium state, so the curve doesn't show obvious detected peak.[32] Fig. 2a and S8† show the galvanostatic discharge curves of CF_x in an aqueous solution of $Zn(CF_3SO_3)_2$. To make the results more intuitive, we used the same current density for different CF_x cathodes in the discharge test. With the cutoff potential of 0.3 V, the corresponding specific capacities were 401, 503, 532, and 74 mA h g^{-1} and energy densities were 297, 388, 317, 26 W h kg^{-1} at the current density of 30 mA h g^{-1}, respectively. A significant initial voltage delay can be observed, which is typically existed in reported CF_x materials.[28,33] The voltage delay of CF_x materials is mainly attributed to their unsatisfactory conductivity.[19] F has the greatest tendency to attract electron density when F and C form a bond, and the electron density is essentially on F, resulting in highly polarized C–F bonds, which result in low intrinsic conductivity of the CF_x material.[34] For a more intuitive representation, Fig. 2b–c and S9† compare the discharge curves of CF_x at the same current density and Fig. S10† shows discharge capacity, energy density, and the corresponding mid-voltage of Zn/CF_x batteries at the current density of 30 mA h g^{-1}. Table S1† details the electrochemical data of Zn/CF_x cells at different current densities. Given the current energy crisis and the demands of commercialization, we have also prepared cathodes with higher active material mass loads. Fig. S11 and Table S2† show the electrochemical discharge curves of CF_x at 30 mA g^{-1} and 500 mA g^{-1}, respectively. With a higher mass loading of 6.3 mg cm^{-2}, the $CF_{0.85}$ still delivered the highest discharge capacity of 455 mA h g^{-1}, which is 90.4% of the previous low mass loading (2.2 mg cm^{-2}). It can be observed that $Zn/CF_{0.85}$ cells perform superior electrochemical performance in discharge capacity, energy density, and power density. The primary cells of various literatures are summarized in Table S3.† Compared with zinc–manganese, zinc–mercury, and zinc–silver batteries, $Zn/CF_{0.85}$ cells have a higher capacity and energy density. Although zinc–air batteries have a high energy density and capacity, they cannot be sealed, causing electrolyte contamination. Compared to Mg/CF_x and Li/CF_x, aqueous electrolyte is cheaper, safer and more environmentally friendly. We also conducted constant current discharge measurements at various temperatures for the $CF_{0.85}$ cathode. Fig. S12† exhibits the discharge curves at different current densities with varied test temperatures. Fig. 2d–e exhibits the discharge curves at 30 and 500 mA g^{-1} with different test temperatures. Indicate that the capacity and cell voltage declined with the decrease in temperature. Fig. 2f shows the corresponding discharge capacity and energy density, and detailed electrochemical data are listed in Table S4.† At the temperature of 50 °C, the battery can deliver a capacity of 550 mA h g^{-1} with an energy density of 457 W h kg^{-1} at the current density of 30 mA g^{-1}. When operated at a commonly-encountered temperature of 0 °C, the cell can deliver a discharge capacity of 460 mA h g^{-1} at the current density of 30 mA g^{-1}, in correspondence to a high retention of about 84% compared to that at 25 °C. To the surprise, a discharge capacity of 347 mA h g^{-1} with a current density of 500 mA g^{-1} at 0 °C can be obtained.

Electrochemical impedance spectroscopy (EIS) is applied to evaluate the interfacial property between the electrode and electrolyte.[35] The impedance spectra were carried out before discharge and are shown in Fig. 3a. All the impedance spectra of CF_x samples present a high-frequency semicircle and a low-frequency tail. The low-frequency tail is a sloping line controlled by the diffusion of the electrode process, and the high-frequency semicircle is a circular arc controlled by the electrochemical step.[36] The impedance spectra are fitted with the equivalent circuit (inset of Fig. 3b) by software, in which the symbols R_b, R_{ct}, Q_{ct}, and Z_{wo} denote the bulk resistance, cell reaction resistance, capacitance of the double layer, and Warburg impedance, respectively.[6,37] Fig. 3b shows the variation of

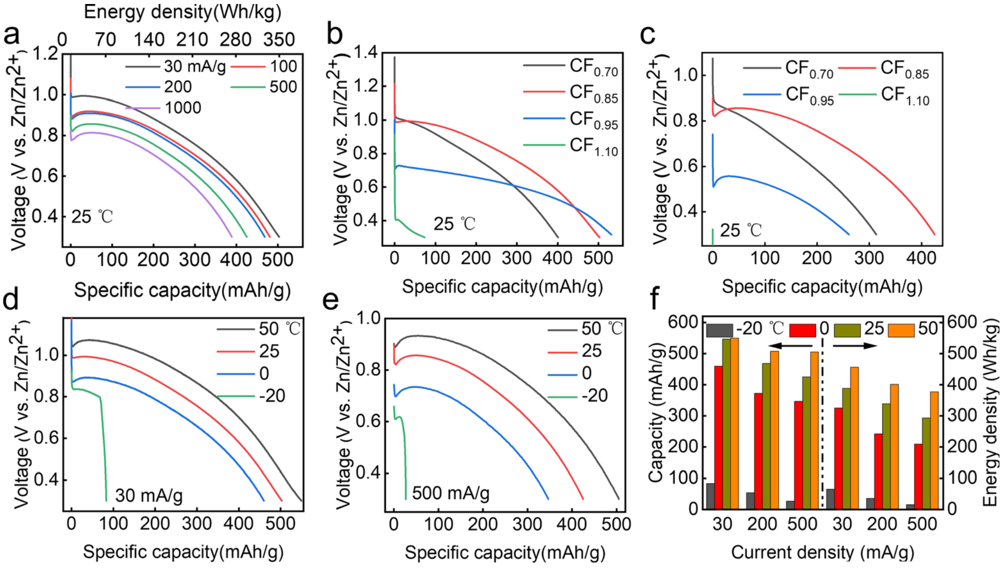

Fig. 2 (a) Galvanostatic discharge plots of the Zn/$CF_{0.85}$ cell at 25 °C, comparison of discharge curves of CF_x at the 25 °C (b) 30 mA g^{-1} and (c) 500 mA g^{-1}. Comparison diagram of Zn/$CF_{0.85}$ battery at different temperatures (d) 30 mA g^{-1}, (e) 500 mA g^{-1}. (f) The corresponding capacity and energy density of the $CF_{0.85}$ sample.

fitted R_{ct} of four CF_x samples. The values of R_{ct} are 417.5, 542.8, 964.4 and 1285 Ω for $CF_{0.70}$, $CF_{0.85}$, $CF_{0.95}$ and $CF_{1.10}$, respectively, the $CF_{0.70}$ exhibits a lower R_{ct} value than other samples. This is attributed to the low fluoride degree of $CF_{0.70}$.

Weppner and Huggins' galvanostatic intermittent titration technique (GITT) has become a standard method for measuring chemical diffusion coefficients in different electrode materials.[38] Herein, to get the insight into the electrochemical kinetics of samples, GITT is used to determine the $D_{Zn}{}^{2+}$ of CF_x as a function of voltage for the entire voltage range of discharge. Fig. 3c shows the discharge curves of CF_x as a function of time. During the GITT measurement, the cell was discharged with

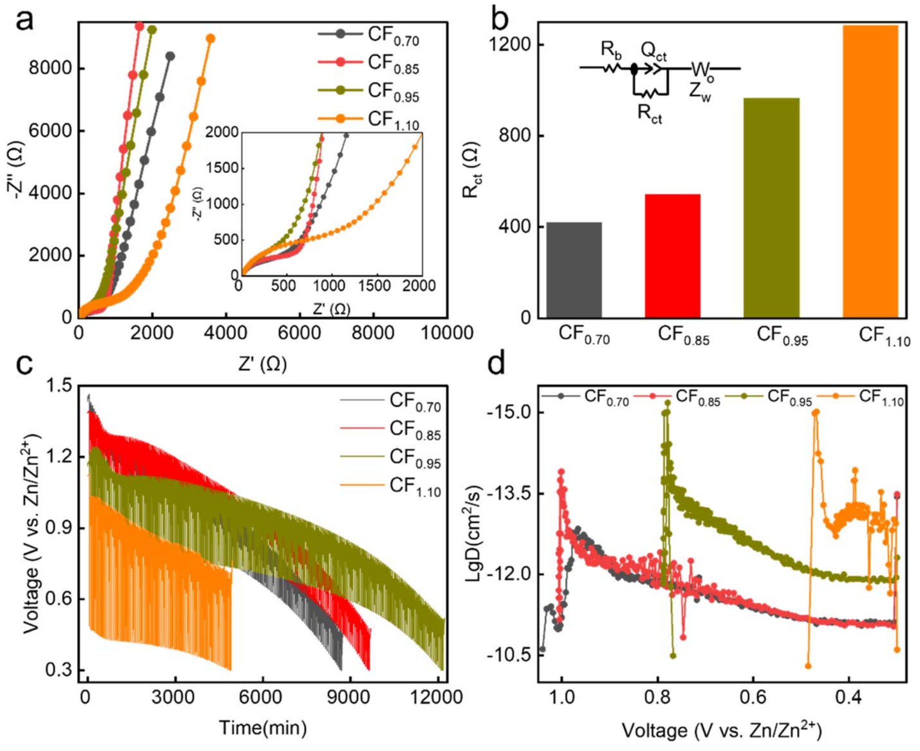

Fig. 3 (a) The impedance spectra, (b) fitted results of R_{ct} measured before discharge. Inset shows the equivalent circuit. (c) The discharge GITT curves of the four samples, (d) the calculated D from the GITT data for four samples as a function of potential during the discharge process.

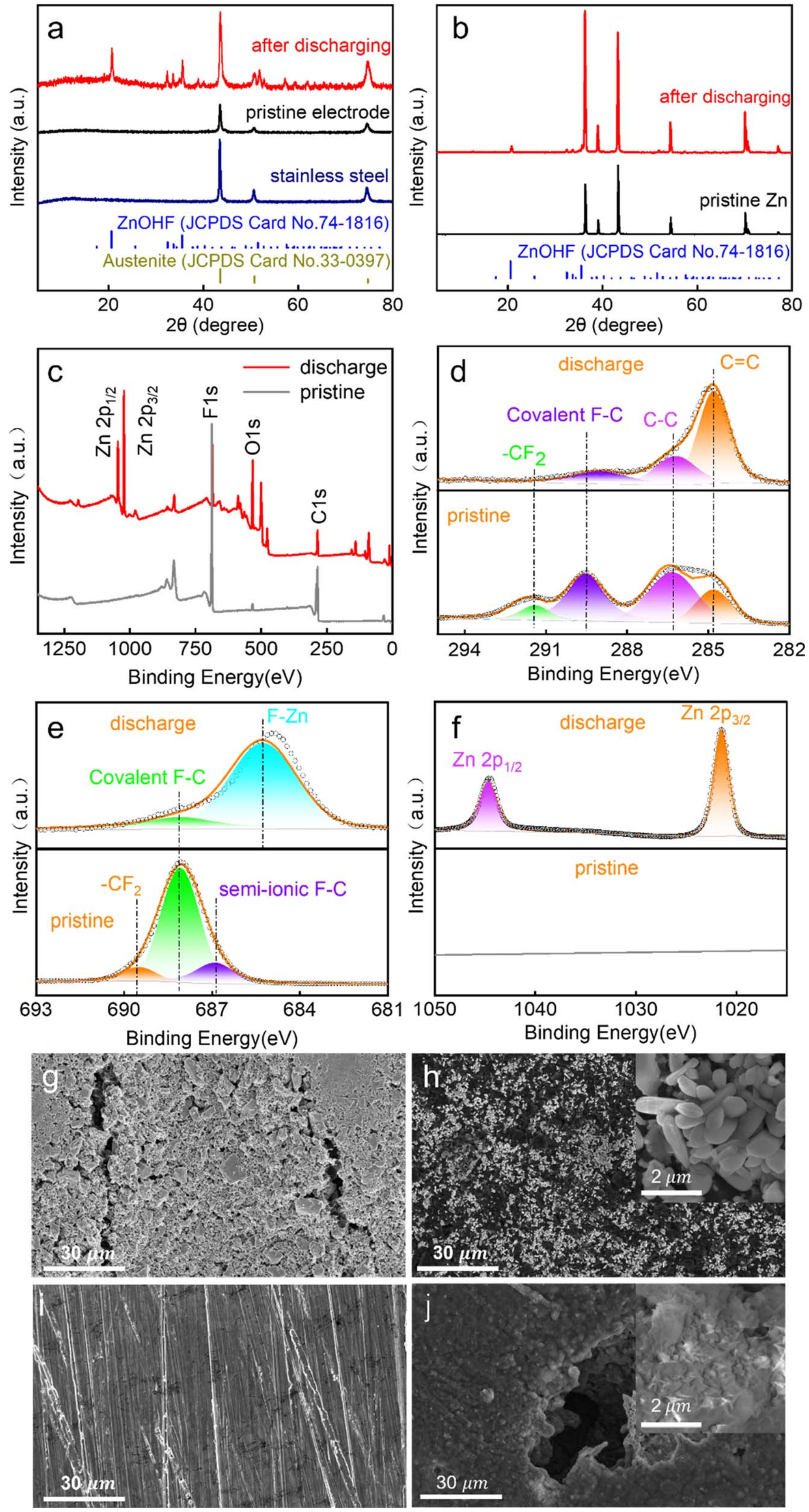

Fig. 4 XRD patterns of the (a) $CF_{0.85}$ sample and (b) Zn discharge at 30 mA g^{-1}. XPS spectrum of (c) survey spectrum; (d) C 1s; (e) F 1s and (f) Zn 2p pristine and after discharge. SEM images of (g) pristine electrode, (h) electrode after discharge at 30 mA g; (i) pristine Zn after polishing; (j) Zn after discharging at 30 mA g^{-1}.

a constant current density of 30 mA g^{-1} for an interval of 5 min, followed by an open circuit stand for 50 min to allow the cell voltage to relax to its steady-state value (E_s) until the voltage of the batteries arrived at 0.3 V. The applied current density and the resulting voltage profile for a single titration during the discharge process is shown in Fig. S13† with schematic labeling of different parameters. Based on the Fick's second law of diffusion, the $D_{Zn^{2+}}$ calculated from the GITT curves as a function of voltage during the discharge process is shown in Fig. 3d. It is found that the $D_{Zn^{2+}}$ value of $CF_{1.10}$ and $CF_{0.95}$ are in the range from ~10^{-10} to ~10^{-15} cm^2 s^{-1}, indicating low kinetics of high fluorination CF_x cathode. However, the $D_{Zn^{2+}}$ value of $CF_{0.70}$ and $CF_{0.85}$ are mainly in the high range from ~$10^{-10.5}$ to ~10^{-14} cm^2 s^{-1}. When the potential drops below 0.97 V, the $D_{Zn^{2+}}$ values of $CF_{0.70}$ and $CF_{0.85}$ will increase to more than ~10^{-13} cm^2 s^{-1} and continues to increase as the potential decreases. When the potential drops below 0.77 V, the same phenomenon occurs in $CF_{0.95}$. This phenomenon implies that the carbon generated improves the conductivity and electrochemical kinetics of the electrodes with the discharge reaction going on.[6]

To further explore the $CF_{0.85}$ electrode reaction mechanism, XRD, XPS, SEM and EDS were measured and analyzed. Fig. 4a shows the XRD patterns of the stainless-steel current collector, $CF_{0.85}$ electrode, and $CF_{0.85}$ electrodes after discharging in the electrolytes of $Zn(CF_3SO_3)_2$ at the current density of 30 mA g^{-1}. When the battery was discharged to 0.3 V, new peaks emerged on the surface of cathode, which could be well assigned to the reflection of ZnOHF (JCPDS Card No.74-1816). Fig. 4b shows the corresponding XRD patterns of the pristine and after discharging anode, indicating that the anode product is also ZnOHF. Different from previous reports, which revealed that the reaction products of Li/CF_x, Na/CF_x, K/CF_x and Mg/CF_x primary cell systems using organic electrolyte are LiF, NaF, KF and MgF_2, respectively.[35,39,40] However, the electrochemical reaction seems to be rather complicated in this research, because the molecule of H_2O also involves in the whole discharge process and which has recognized as a common phenomenon in the existed aqueous zinc primary batteries.[41–43] The survey spectrum of the electrodes before and after discharge is shown in Fig. 4c, the spectrum of the pristine electrode is basically consistent with $CF_{0.85}$ powder, while the discharged electrode shows the typical XPS spectrum of ZnOHF.[44] In the C 1s spectrum (Fig. 4d), there are three peaks after discharge, mainly C=C bonds, with only a few C–F bond. The peaks of F 1s had an additional peak at 684.7ev, corresponding to F–Zn.[45] Fig. 4f shows the Zn 2p spectrum, where the two peaks of binding energy 1044.5ev and 1021.4ev correspond to Zn $2p_{1/2}$ and Zn $2p_{3/2}$, respectively.[46]

Consequently, the overall discharge reaction of the Zn/CF_x battery can be proposed as follows:

$$2CF_x + xZn^{2+} + xZn + 2xH_2O \rightarrow 2C + 2xZnOHF + 2xH^+$$

Fig. 4g and h demonstrate that after discharging to 0.3 V in $Zn(CF_3SO_3)_2$, the surface of the $CF_{0.85}$ electrode is covered with white rice-like particles. The changes of the surface roughness before and after discharge further confirmed the formation of reaction products on the surface of electrode. Fig. 4i and j show that the corresponding zinc anode surface is covered with dense particle layers after discharging. This phenomenon implied the formation of new substances on the surface of both cathode and anode, indicating the occurrence of electrochemical reactions. The atomic compositions of discharged $CF_{0.85}$ are shown in Fig. S14.† The average molar concentration ratio of O, F, and Zn elements in $CF_{0.85}$ electrode and zinc anode after discharging were 18.48 : 25.75 : 17.40 and 31.76 : 36.23 : 29.44 (Table S5†). The molar ratio of O : F : Zn was generally consistent with the stoichiometric ratio of ZnOHF chemical formula and in which the slightly more F element may be caused by the untreated clean residual F from the electrolyte. The EDS spectroscopy results were consistent with the XRD phase characterization results described above. These results confirmed that the electrochemical reaction of $CF_{0.85}$ with zinc in $Zn(CF_3SO_3)_2$ produces ZnOHF during the discharging process.

4. Conclusions

In conclusion, CF_x were used as the cathode material for aqueous zinc primary batteries for the first time, which is a novel application. The electrochemical performance of these batteries was tested using $Zn(CF_3SO_3)_2$ electrolyte. Among the four CF_x samples, $CF_{0.85}$ exhibited the best electrochemical performance. The $Zn/CF_{0.85}$ cell showed a mid-voltage of 0.81 V and a high discharge capacity of 503 mA h g^{-1} up to 0.3 V. The final products of this reaction were ZnOHF and C. This research not only provides valuable insights into the properties of fluorinated carbon, but also opens up new avenues for the development of commercialized aqueous zinc primary batteries that offer high energy density, low cost, and high safety. It has the potential to power a variety of electronic devices in the consumer industry, such as watches, cameras, toys, and remote controls.

Conflicts of interest

There are no conflicts to declare.

Acknowledgements

This work was financially supported by the Natural Science Foundation of Xiamen City (3502Z202371033), and XMIREM autonomously deployment project (No.2023CX15).

References

1 Z. Fang, Y. Peng, X. Zhou, L. Zhu, Y. Wang, X. Dong and Y. Xia, Fluorinated Carbon Materials and the Applications in Energy Storage Systems, *ACS Appl. Energy Mater.*, 2022, **5**, 3966–3978.

2 N. Sharma, M. Dubois, K. Guérin, V. Pischedda and S. Radescu, Fluorinated (Nano)Carbons: CF_x Electrodes and CF_x-Based Batteries, *Energy Technol.*, 2021, **9**(4), 2000605.

3 M. Adamska and U. Narkiewicz, Fluorination of Carbon Nanotubes – A Review, *J. Fluorine Chem.*, 2017, **200**, 179–189.

4 J.-C. Agopian, O. Teraube, K. Charlet and M. Dubois, A review about the fluorination and oxyfluorination of carbon fibres, *J. Fluorine Chem.*, 2021, **251**, 109887.

5 S. Ha, C. Lim and Y.-S. Lee, Fluorination methods and the properties of fluorinated carbon materials for use as lithium primary battery cathode materials, *J. Ind. Eng. Chem.*, 2022, **111**, 1–17.

6 Z. Luo, D. Chen, X. Wang, J. Huang, Y. Pan, W. Lei and J. Pan, Accordion-Like Fluorinated Graphite Nanosheets with High Power and Energy Densities for Wide-Temperature, Long Shelf-Life Sodium/Potassium Primary Batteries, *Small*, 2021, **17**, e2008163.

7 W. Liu, H. Li, J. Y. Xie and Z. W. Fu, Rechargeable room-temperature CF_x-sodium battery, *ACS Appl. Mater. Interfaces*, 2014, **6**, 2209–2212.

8 H. Yue, H. Chen, C. Zhao, Z. Zheng, K. Zhou, Q. Zhang, G. Zhong, C.-Z. Lu and Y. Yang, Reversible potassium storage in ultrafine CF : A superior cathode material for potassium batteries and its mechanism, *J. Energy Chem.*, 2021, **53**, 347–353.

9 J. Vatsala Rani, S. Bhavana Rushi, V. Kanakaiah and S. Palaniappan, Green Fluorination of Natural Graphite and its Application in Rechargeable Magnesium Ion Transfer Battery, *J. Electrochem. Soc.*, 2011, **158**(9), A1031.

10 N. Wang, H. Wan, J. Duan, X. Wang, L. Tao, J. Zhang and H. Wang, A review of zinc-based battery from alkaline to acid, *Mater. Today Adv.*, 2021, **11**, 100149.

11 X. Jia, C. Liu, Z. G. Neale, J. Yang and G. Cao, Active Materials for Aqueous Zinc Ion Batteries: Synthesis, Crystal Structure, Morphology, and Electrochemistry, *Chem. Rev.*, 2020, **120**, 7795–7866.

12 W. Shang, W. Yu, Y. Liu, R. Li, Y. Dai, C. Cheng, P. Tan and M. Ni, Rechargeable alkaline zinc batteries: Progress and challenges, *Energy Storage Mater.*, 2020, **31**, 44–57.

13 Y. Zhang, Y. Zhang, A. Mathur, S. Ben-Yoseph, S. Xia, Y. Wu and N. Liu, An effective and accessible cell configuration for testing rechargeable zinc-based alkaline batteries, *J. Power Sources*, 2021, **491**, 229547.

14 D. Kundu, S. Hosseini Vajargah, L. Wan, B. Adams, D. Prendergast and L. F. Nazar, Aqueous vs. nonaqueous Zn-ion batteries: consequences of the desolvation penalty at the interface, *Energy Environ. Sci.*, 2018, **11**, 881–892.

15 Y. Hattori, K. Kaneko, F. Okino, H. Touhara, T. Kyotani and A. Tomita, Adsorptive properties of designed fluorinated carbon nanotubes, *Adsorption Science and Technology*, World Scientific, 2000, pp. 309–313.

16 X. Chen, K. Fan, Y. Liu, Y. Li, X. Liu, W. Feng and X. Wang, Recent Advances in Fluorinated Graphene from Synthesis to Applications: Critical Review on Functional Chemistry and Structure Engineering, *Adv. Mater.*, 2022, **34**, e2101665.

17 Y. Kita, N. Watanabe and Y. Fujii, Chemical composition and crystal structure of graphite fluoride, *J. Am. Chem. Soc.*, 1979, **101**, 3832–3841.

18 G. A. Shia and G. Mani, Fluorinated Carbon, in *Organofluorine Chemistry: Principles and Commercial Applications*, R. E. Banks, B. E. Smart and J. C. Tatlow, ed. Springer US, Boston, MA, 1994, pp. 483–499.

19 C. Peng, Y. Li, F. Yao, H. Fu, R. Zhou, Y. Feng and W. Feng, Ultrahigh-energy-density fluorinated calcinated macadamia nut shell cathodes for lithium/fluorinated carbon batteries, *Carbon*, 2019, **153**, 783–791.

20 P. Meduri, H. Chen, J. Xiao, J. J. Martinez, T. Carlson, J. G. Zhang and Z. D. Deng, Tunable electrochemical properties of fluorinated graphene, *J. Mater. Chem. A*, 2013, **1**, 7866–7869.

21 S. Yan, Y. Yuan, W. Xu, X. Yao, X. Chen, S. Liu and J. Zhao, Structure and strippability of graphite fluoride treated with concentrated alkaline solution, *J. Fluorine Chem.*, 2019, **225**, 21–26.

22 S. Jiang, P. Huang, J. Lu and Z. Liu, The electrochemical performance of fluorinated ketjenblack as a cathode for lithium/fluorinated carbon batteries, *RSC Adv.*, 2021, **11**, 25461–25470.

23 J. Giraudet, C. Delabarre, K. Guérin, M. Dubois, F. Masin and A. Hamwi, Comparative performances for primary lithium batteries of some covalent and semi-covalent graphite fluorides, *J. Power Sources*, 2006, **158**, 1365–1372.

24 W. Feng, P. Long, Y. Feng and Y. Li, Two-dimensional fluorinated graphene: synthesis, structures, properties and applications, *Advanced Science*, 2016, **3**, 1500413.

25 C. Sun, Y. Feng, Y. Li, C. Qin, Q. Zhang and W. Feng, Solvothermally exfoliated fluorographene for high-performance lithium primary batteries, *Nanoscale*, 2014, **6**, 2634–2641.

26 Z. Li, X. Li, L. Zhou, Z. Xiao, S. Zhou, X. Zhang, L. Li and L. Zhi, A synergistic strategy for stable lithium metal anodes using 3D fluorine-doped graphene shuttle-implanted porous carbon networks, *Nano Energy*, 2018, **49**, 179–185.

27 W. Wang, Y. Li, Y. Feng, J. Han, F. Zhang, P. Long, C. Peng, C. Cao, Y. Cao and H. Yang, Asymmetric self-supporting hybrid fluorinated carbon nanotubes/carbon nanotubes sponge electrode for high-performance lithium-polysulfide battery, *Chem. Eng. J.*, 2018, **349**, 756–765.

28 X.-X. Yang, G.-J. Zhang, B.-S. Bai, Y. Li, Y.-X. Li, Y. Yang, X. Jian and X.-W. Wang, Fluorinated graphite nanosheets for ultrahigh-capacity lithium primary batteries, *Rare Met.*, 2021, **40**, 1708–1718.

29 N. Chen, G. Zhang, H. Chen and H. Yue, Conductive Carbon-Wrapped Fluorinated Hard Carbon Composite as High-Performance Cathode for Primary Lithium Batteries, *Coatings*, 2023, **13**(5), 812.

30 K. Guérin, M. Dubois, A. Houdayer and A. Hamwi, Applicative performances of fluorinated carbons through fluorination routes: A review, *J. Fluorine Chem.*, 2012, **134**, 11–17.

31 G. Fang, J. Zhou, A. Pan and S. Liang, Recent Advances in Aqueous Zinc-Ion Batteries, *ACS Energy Lett.*, 2018, **3**, 2480–2501.

32 S. Aderyani, P. Flouda, S. Shah, M. Green, J. Lutkenhaus and H. Ardebili, Simulation of cyclic voltammetry in structural

supercapacitors with pseudocapacitance behavior, *Electrochim. Acta*, 2021, **390**, 138822.

33 D. Zhu, J. Yuan, T. Wang, Y. Dai, Y. Peng, W. Li, A. Li and J. Zhang, A novel one-step method to prepare N, S Co-doped sub-fluorinated carbon electrode materials for ultrahigh-rate lithium-fluorinated carbon battery, *J. Power Sources*, 2022, **551**, 232188.

34 J. Ma, Y. Liu, Y. Peng, X. Yang, J. Hou, C. Liu, Z. Fang and X. Jian, UV-radiation inducing strategy to tune fluorinated carbon bonds delivering the high-rate Li/CF$_x$ primary batteries, *Composites, Part B*, 2022, **230**, 109494.

35 X. Miao, J. Yang, W. Pan, H. Yuan, Y. Nuli and S.-i. Hirano, Graphite fluoride as a cathode material for primary magnesium batteries with high energy density, *Electrochim. Acta*, 2016, **210**, 704–711.

36 X. Y. Zhao, J. P. Tu, Y. Lu, J. B. Cai, Y. J. Zhang, X. L. Wang and C. D. Gu, Graphene-coated mesoporous carbon/sulfur cathode with enhanced cycling stability, *Electrochim. Acta*, 2013, **113**, 256–262.

37 Y. Li and W. Feng, The tunable electrochemical performances of carbon fluorides/manganese dioxide hybrid cathodes by their arrangements, *J. Power Sources*, 2015, **274**, 1292–1299.

38 C. Chen, Z. Zhang, J. Cao, H. Meng and C. Yanying, Stable layered Ni-rich LiNi0.9Co0.07Al0.03O2 microspheres assembled with nanoparticles as high-performance cathode materials for lithium-ion batteries, *J. Mater. Chem. A*, 2017, **5**, 2724–2731.

39 P. Chen, B. Wang, Z. Wu, X. Niu, C. Ouyang, H. Li and L. Wang, Fluorinated soft carbon as an ultra-high energy density potassium-ion battery cathode enabled by a ternary phase KFC, *J. Energy Chem.*, 2023, **77**, 38–44.

40 Y.-Y. Li, C. Liu, L. Chen, X.-Z. Wu, P.-F. Zhou, X.-Y. Shen and J. Zhou, Multi-layered fluorinated graphene cathode materials for lithium and sodium primary batteries, *Rare Met.*, 2022, **42**, 940–953.

41 K. Kordesch and W. Taucher-Mautner, *Leclanchè and Zinc-Carbon, Encyclopedia of Electrochemical Power Sources*, Elsevier BV, 2009, pp. 43–54.

42 H. Arai and M. Hayashi, Primary batteries–AQUEOUS SYSTEMS| zinc–air, *Encyclopedia of Electrochemical Power Sources*, 2009, pp. 55–61.

43 K. Kordesch and W. Taucher-Mautner, PRIMARY BATTERIES – AQUEOUS SYSTEMS | Zinc–Mercury, in *Encyclopedia of Electrochemical Power Sources*, J. Garche, ed. Elsevier, Amsterdam, 2009, pp. 62–67.

44 X. Zong, C. Sun, H. Yu, Z. G. Chen, Z. Xing, D. Ye, G. Q. Lu, X. Li and L. Wang, Activation of Photocatalytic Water Oxidation on N-Doped ZnO Bundle-like Nanoparticles under Visible Light, *J. Phys. Chem. C*, 2013, **117**, 4937–4942.

45 M. Dai, F. Xu, Y. Lu, Y. Liu and Y. Xie, Synthesis of submicron rhombic ZnO rods via ZnOHF intermediate using electrodeposition route, *Appl. Surf. Sci.*, 2011, **257**, 3586–3591.

46 Q.-L. Huang, M. Wang, H.-X. Zhong, X.-T. Chen, Z.-L. Xue and X.-Z. You, Netlike nanostructures of Zn (OH) F and ZnO: synthesis, characterization, and properties, *Cryst. Growth Des.*, 2008, **8**, 1412–1417.